Non-conventional arrays for self-potential surveys

Oziel Souza de Araújo [1,2] Samuel Butler,[3] Stefano Picotti,[1] Roberto G. Francese,[1,2] Carlos Alberto Mendonça,[4] Federico Fischanger[5] and Massimo Giorgi[1]

[1]*National Institute of Oceanography and Applied Geophysics (OGS), Borgo Grotta Gigante, 42/c, 34010 Sgonico TS, Italy.*
E-mail: oziel.souzadearaujo@unipr.it, osouzadearaujo@ogs.it
[2]*Department SCVSA, University of Parma, Parco Area delle Scienze, 11/a, Parma, PR 43124, Italy*
[3]*Department of Geology, University of Saskatchewan, 114 Science Place, Campus Drive, Saskatoon, SK S7N 5E2, Canada*
[4]*Department of Geophysics, University of São Paulo, Rua do Matão, 1226, Sao Paulo, SP CEP 05508-090, Brazil*
[5]*GEG Experts Sas, Av. du Champ de Mars, Le Lab'O, Orléans, 45100, France*

SUMMARY
The exponential growth of electrical resistivity tomography (ERT) methods for exploring the subsurface at large depths widened the applicability of the self-potential (SP) method, a passive geoelectrical technique suitable for a variety of purposes like mapping ore bodies or inferring fluid flow in the subsurface. Several new-generation resistivity meters have been designed to continuously log the electric potentials thus allowing for the identification of weak amplitude signals and resulting in deeper inversion models. In such approaches, long SP time-series are collected but are totally ignored as only marginal intervals are retained and analysed in the ERT procedure. The discarded SP records could be valuable although not collected using the traditional methodology, based on a reference electrode. We present an SP forward modelling feasibility study of different array techniques, based on numerical finite-element methods. The SP has been modelled in a variety of electrical settings to assess the imaging potentials of non-conventional (i.e. sparse gradient and full sparse gradient) arrays in comparison to traditional (i.e. fixed-base and the leapfrog) arrays. The analytic signal amplitude (ASA) algorithm was employed to compare numerical modelling results obtained from the different type of arrays, highlighting the great potentials of non-conventional arrays for the recognition of several sources of SP anomalies. The ASA maps, presenting a single peak centred over the targets, can significantly help in identifying the source anomalies for all the analysed array techniques. The cost-effectiveness along with the imaging capability of these non-conventional arrays constitute important benefits that could be exploited resulting in a systematic inclusion of SP analysis when collecting deep ERT data using distributed systems.

Key words: Electrical properties; Electrical resistivity tomography (ERT); Numerical modelling.

1 INTRODUCTION

The self-potential (SP) method is a passive geoelectrical technique that is particularly sensitive to the presence of ore bodies (Mehanee 2014; Rakoto *et al.* 2019; Su *et al.* 2022; Zhu *et al.* 2023; Revil *et al.* 2023b) and to the movement of fluids in the subsurface (Poldini 1938; Sill 1983; Jouniaux *et al.* 2009; Valois *et al.* 2018; Ahmed *et al.* 2020; Kukemilks & Wagner 2021). There are several examples in the literature describing the application of the SP method like hydrogeophysics (Revil *et al.* 2006; Jouniaux *et al.* 2009), mineral exploration (Biswas 2017), dykes and embankments (Song *et al.* 2021), quantitative analysis (Eppelbaum 2021), hydrothermal systems (Finizola *et al.* 2004; Revil *et al.* 2023a) and marine exploration (Xie *et al.* 2023). Although collecting SP data is quite simple,

its systematic use has been fairly limited by lack of a quantitative approach and uncertainties in data interpretation (Nyquist & Corry 2002; Revil & Jardani 2013; Barde-Cabusson *et al.* 2021). Further limitations depend on the absence of a definitive consensus on data inversion procedures.

This scenario has been partly changed because of the recent growing use of electrical resistivity methods to explore the subsurface at large depths (deep electrical resistivity tomography—DERT), in a variety of geological conditions (Carrier *et al.* 2019; Lajaunie *et al.* 2019; Troiano *et al.* 2019). DERT surveying boosted the use and the development of distributed systems as an effective alternative to traditional resistivity meters. Distributed systems are based on the separation of transmitting and receiving units (Lajaunie *et al.* 2019; Bocchia *et al.* 2021) and they use powerful or multiple transmitters

to increase the signal-to-noise ratio at large depths. The receivers are often comprised of recorders capable of continuously sampling, at high frequency, the natural and artificial electric potentials. The FullWaver (Gance *et al.* 2018) and the Multisource (LaBrecque *et al.* 2013; Picotti *et al.* 2017; Bocchia *et al.* 2021) are among these new generation resistivity meters and they allow for the deployment of complicated patterns of receiving electrodes and also for the permanent storage of long time-series of electric potentials. Following the standard DERT procedure, the natural SP values in these data sets are treated as noise rather than signal and they are filtered out to retrieve the artificial potentials. Contrarily, these SP data, when adequately processed, represent a valuable geophysical signal useful to map specific geological features in the subsurface. The lack of logistical constraints while deploying the distributed systems for DERT purposes enables to adopt a non-conventional type of SP array, herein referred to as the sparse gradient (SG) array, which is explained in the following sections. This uncommon type of array consists of several sparse dipoles with independent units logging the potential difference (p.d.) between couples of electrodes. In order to evaluate the SG technique, we thus consider a base-measuring pattern consisting of two-channel recorders connected to three electrodes that simultaneously sample two values of p.d. There are numerous studies in the literature adopting multichannel self-potential measurements in offshore surveys (Ikard *et al.* 2021; Zhu *et al.* 2021, 2023; Song *et al.* 2022; Su *et al.* 2022; Jiang *et al.* 2024). In contrast, the SG technique represents a significantly different approach, as there are no common reference electrodes for all measurements, and the acquisition is performed onshore. The 'star network' approach presented by Revil & Jardani (2013) is somewhat similar to the full SG approach, because it exploits the p.d. between electrodes controlled by a set of base stations deployed in an 'L-shaped form,' with the units separated by several hundred metres. To our knowledge, in the literature there are no other examples regarding the employment of the SG technique, as well as on the data interpretation, for SP studies.

Several studies in the literature applied numerical, analytical and graphical methods to generate synthetic SP data, with the purpose of interpreting SP anomalies (Meiser 1962; Paul 1965; Rao *et al.* 1970; Monteiro Santos 2010; Roudsari & Beitollahi 2013; Xie *et al.* 2020). Some of these works adopted the COMSOL Multiphysics package, which is a computational modelling software based on the finite-element methods to solve partial differential equations (e.g. Boleve *et al.* 2007; Soueid Ahmed *et al.* 2016; Troiano *et al.* 2017; Ahmed *et al.* 2020; Kang *et al.* 2020). Among the analytical and graphical methods, the analytic signal amplitude (ASA) algorithm uses gradients and the fast Fourier transform (FFT) to generate potential field maps (Abdelrahman *et al.* 2003, 2009), which contributes to better estimate the source location. This technique has been commonly applied (e.g. Sundararajan & Srinivas 1996; Sundararajan *et al.* 2000) to effectively locate source anomalies for geophysical methods based on potential fields (e.g. magnetic and gravimetric). ASA approach, for SP surveying, has been successfully applied in many studies (e.g. Atchuta Rao & Ram Babu 1983; Agarwal 1984; Sundararajan & Srinivas 1996; Agarwal & Srivastava 2009; Mehanee *et al.* 2023). The normalized full gradient technique has been also utilized (Sundararajan *et al.* 1998; Sindirgi *et al.* 2008; Abedi *et al.* 2012; Sindirgi & Ozyalin 2019) integrating ASA with the downward continuation.

Two standard single-channel techniques have been widely reported in the literature for SP data acquisition: the potential or fixed-base and the gradient (leapfrog). Theoretically, under some circumstances, they are somewhat equivalent but, from the

practical point of view, they are rather different (Orellana 1972). Unfortunately, over large scales these standard approaches are not cost-effective. Data quality is generally high, but site logistics and acquisition time often result in expensive surveys and poor subsurface coverage.

The SG technique could take advantage of the multichannel capability of the new generation resistivity meters. However, most SP surveys still use the standard techniques rather than the SG ones, because the hardware for single-channel SP measurements is relatively cheap. For this reason, to our knowledge, SG arrays has not been sufficiently explored for SP surveys, although current technology is sufficiently mature to switch from single to multichannel measurements. New-generation multichannel resistivity meters could notably speed up the recording, facilitating the deployment also in the case of complicate acquisition geometry.

Initial attempts to invert SP measurements in a background resistivity model were based on the calculation of the charge occurrence probability function (Patella 1997). Other authors solve the SP inversion after calculating the distribution of streaming current sources in specific hydraulic settings using the Poisson's equations (Jardani *et al.* 2006; Minsley *et al.* 2007; Sheffer & Oldenburg 2007), and devised similar or alternative approaches (Mendonça 2008; Revil & Jardani 2013). Generally, it appears that a robust procedure (Gibert & Sailhac 2008; Revil *et al.* 2008; Auken *et al.* 2010; Revil 2010) has not yet developed, and for this reason the SP surveys are often combined with other geophysical methods for localizing groundwater flows and pollutant plumes, as well as for quantifying pertinent hydraulic properties of aquifers (e.g. Jouniaux *et al.* 2010).

In this contribution, we provide a qualitative analysis of SP techniques through synthetic modelling, showing how meaningful can be the information extracted from data obtained using both conventional and non-conventional arrays, that is, the SG array. We also report here about SP forward modelling based on finite-element numerical methods, to compare the responses of different arrays. We also present an SP analysis, based on the ASA algorithm, to evaluate the effectiveness and suitability of new-generation resistivity meters employing SG arrays to reconstruct different sources of anomalies.

2 BASIC THEORY

2.1 Self-potential forward modelling

We assume a homogeneous medium, under the hypothesis of the stationarity of currents. Since the charge is conserved, in the low-frequency limit the total current density J (A m^{-2}) must satisfy the continuity equation

$$\nabla \cdot J = 0, \tag{1}$$

(e.g. Griffiths 1999). Moreover, the following two equations hold

$$J = \sigma E + J_s, \tag{2}$$

$$E = \left(E_x, E_y, E_z\right) = -\nabla V, \tag{3}$$

where σ is the electric conductivity (S m^{-1}), E (V m^{-1}) is the quasi-static electric field and V is the electric potential (V). Furthermore, $J_c = \sigma E$ represents the conduction current density in the material,

while J_s denotes the source current density. Therefore, the continuity eq. (1) implies

$$\nabla \cdot \sigma \nabla V = \nabla \cdot J_s = Q_s , \qquad (4)$$

(e.g. Zhu *et al.* 2023), where Q_s represents the current source in the unit volume (in $A\,m^{-3}$). Eq. (4) is the equation governing the SP forward modelling.

The outer boundaries are insulating and so have no net flux, that is, the sum of all point current sources must be zero, as required by the stationary condition. The distance of the model boundaries from the area of interest is assumed large enough that it does not affect the numerical solution.

To find numerical solutions of the above problem, we used the COMSOL Multiphysics package (AB COMSOL 2017), which is a computational modelling software based on the finite-element methods to solve partial differential equations. In COMSOL, the simulation domain is discretized into a grid of finite elements. The software uses a series of pre-determined form functions for most finite elements that describe how the values vary within each element. They are mathematical functions aiding in the numerical approximation of solutions to the equations within the finite-element method. By defining the nodes and using the functions, COMSOL is able to interpolate the intermediate values within each finite element.

2.2 Analytical signal amplitude

The ASA technique, commonly used in magnetic and gravimetric methods, can help to identify the primary source of SP. Following Nabighian (1972), Roest *et al.* (1992), Biswas (2019) and Sindirgi & Ozyalin (2019), the 3-D analytic signal (or ASA) of a potential field is defined as:

$$ASA = \left[\left(\frac{\partial V}{\partial x} \right)^2 + \left(\frac{\partial V}{\partial y} \right)^2 + \left(\frac{\partial V}{\partial z} \right)^2 \right]^{1/2} , \qquad (5)$$

where V represents either the simulated (or measured) potential or p.d. at the surface. In the case of electric potential field, as defined in eq. (3), the three derivatives in eq. (5) coincide with the three components E_x, E_y and E_z, that is, the ASA is the modulus of the electric field E or the total gradient magnitude V of the SP anomaly. Since our data are computed at a flat surface, E_z in eq. (3) is zero. The potential derivatives in eq. (5) can be computed numerically by using the FFT technique. The ASA technique first calculates the analytic signal of the input profile using a Hilbert transform. Then, local peaks in the analytic signal profile are interpreted as corners of source bodies, and the shape of the peak contains information about the depth of the corner (Li 2006; Beiki 2010; Sunny 2018). The ASA tends to show a single peak centred over the source anomaly. In absence of aliasing with a sufficient signal-to-noise ratio, ASA allows for an accurate horizontal localization of anomalies.

3 NUMERICAL EXAMPLES

Our study considers conductive anomalies of different geometry embedded in a uniform medium with background resistivity of 50 Ω·m. The total volume, discretized by a tetrahedral mesh, is a 400 m high parallelepiped, with a base area of 1 km² (Fig. 1a).

Cylindrical, spherical or blocky anomalies were all tested. The cylindrical body, with a radius of 5 m, is 40 m long. It has a resistivity of 10 Ω·m and can be vertical, dipping 35° to the positive *X*-direction

or dipping 35° to the negative *Y*-direction (Fig. 1b). The spherical body, with a resistivity of 10 Ω·m, has either a radius of 10 or 40 m (Fig. 1c). The cylinder and the sphere are centred at $(X, Y, Z) = (0, 0, 170)$. Then five 8 m³ blocks, with a resistivity of 90 Ω·m, were placed at 5 and 10 m depth, as shown in Fig. 1(d). A total of 180 survey points (i.e. electrode positions) are deployed at the surface along 10 lines. Each line comprises six sets of acquisition units, 30 m spaced and labelled from A to F, as shown in Fig. 1(d). Each unit has two channels and it controls three electrodes (i.e. two dipoles), 20 m spaced (Fig. 1d). All array techniques presented here adopt the same electrode deployment However, as will be seen in the following sections, the arrangement in triplets applies only to the unconventional arrays that will be presented, such as the SG technique, which comprises three electrodes or two dipoles for each unit of measurement.

The spherical anomaly is divided into eight equally spaced longitudes and two lines of constant latitude (Fig. 1c). We placed a negative and a positive point source of 50 mA at the poles (top and bottom, respectively), and eight negative point sources of −25 mA on the top line of constant latitude, and other eight positive point sources of 25 mA on the bottom line of constant latitude. Regarding the cubic blocks, a point source of 5 mA (absolute value) was added at each corner, that is, four negative point sources at top and four positive point sources at the bottom for each block. The cylindrical body is divided into two parts, with four equally spaced point sources of −50 mA at the top face and +50 mA at the bottom face. At a distance of 20 m from the top and the bottom, other eight equally spaced positive and eight negative point sources of 25 mA were placed around the cylinder, as shown in Fig. 1(b). In all models, the current sources summation is 0.

The mesh was built with a maximum element size of 10 m, minimum element size of 0.2 m and a curvature factor of 0.2 m. The mesh was refined around every point source and every electrode position at surface, thus increasing the resolution in the regions of interest (Fig. 1a).

3.1 Fixed-base technique

The Fixed-base technique consists in computing the p.d. with respect to a fixed reference electrode. Fig. 1(d) shows a reference electrode (labelled as L10A2) located away from the cylindrical anomaly, giving a sequence of p.d. shown in Table 1.

Considering the electric potential in L10A2 at ground level (0 mV), the electric potential of the other electrodes is equal to the measured p.d. In other words, the L10A2 point is taken as reference electrode in all fixed-base simulations.

3.2 Leapfrog technique

The gradient or leapfrog technique is displayed in Fig. 2, and corresponds to a sequential p.d. for each dipole as shown in Table 2.

A modified leapfrog technique is obtained by setting the potential at position L10A2 at ground level (0 mV), and referring all the p.d. to this reference electrode. This means that the potential at point A1 in line 10 (L10A1) equals the measured p.d. V1. Then, the p.d. V2 is equal to the potential at point A3 in line 10 (L10A3), which implies:

$$V3 = L10B1 - V2, \qquad (6)$$

$$L10B1 = V2 + V3, \qquad (7)$$
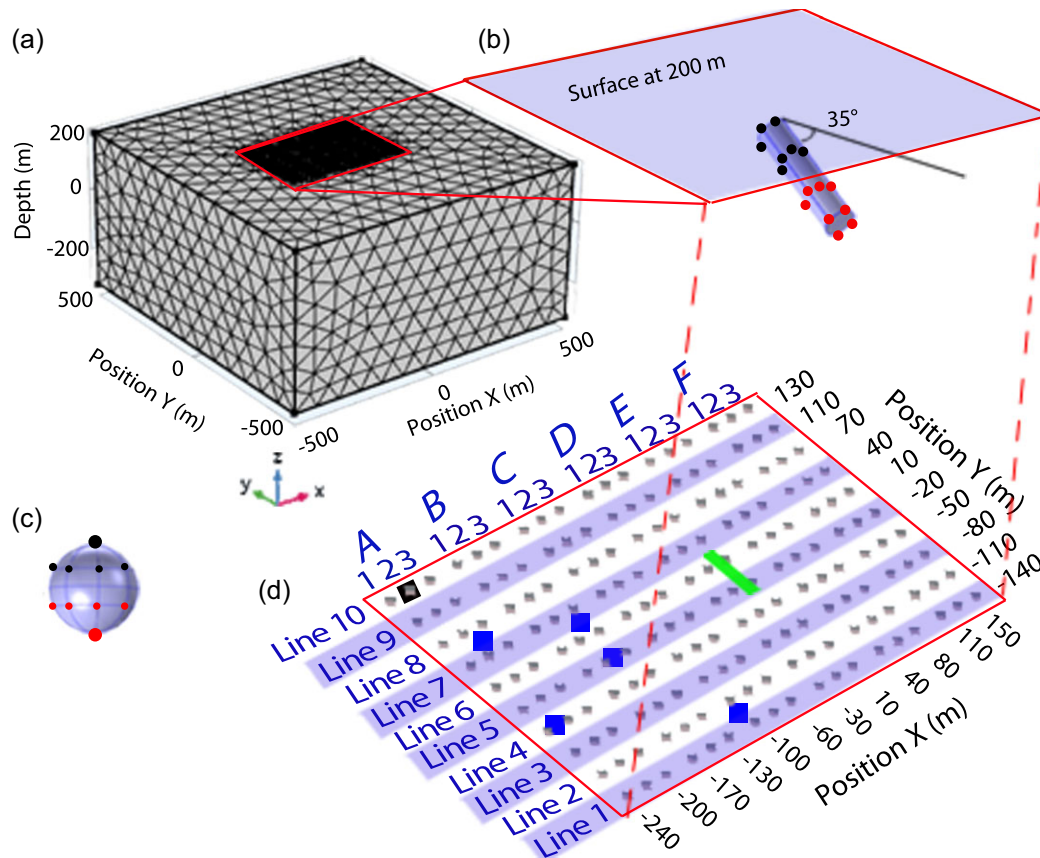
Figure 1. (a) Discretized COMSOL model; (b) cylindrical conductive anomaly dipping 35° to the negative *Y*-direction, where black and red dots are negative and positive current sources, respectively; (c) spherical conductive anomaly with corresponding current sources; (d) acquisition pattern with 180 electrodes separated by 10 lines (30 m spaced along *Y*) and six acquisition units (from A to F, 70 m spaced along *X*). Each unit controls three electrodes (two channels), 20 m spaced. The square in unit A2 is a reference electrode, labelled as L10A2, meaning 'line 10', position A2. The filled squares (line 2, and lines 4 to 8) are blocky conductive anomalies. The rectangle is the projection of the cylindrical conductive anomaly on the surface.

Table 1. Sequential p.d. in the Fixed-based technique, using the reference electrode L10A2, for lines 10 and 9 labelled as L10 and L9, respectively.

| Potential difference	Potentials
V1	L10A1–L10A2
V2	L10A2–L10A2
V3	L10A3–L10A2
V4	L10B1–L10A2
V5	L10B2–L10A2
V6	L10B3–L10A2
...	...
V19	L10F3–L10A2
V20	L9A1–L10A2
V21	L9A2–L10A2
V22	L9A3–L10A2
V23	L9B1–L10A2
V24	L9B2–L10A2
...	...

$$V4 = L10B2 - L10B1. \qquad (8)$$

Substituting eq. (7) in eq. (8):

$$L10B2 = V4 + L10B1 = V2 + V3 + V4, \qquad (9)$$

and so on. In other words, in the leapfrog technique we can sum successive p.d. to infer the electric potential in each point. For this reason, this technique is referred to as 'leapfrog with summation'.

2.3 The SG technique

As introduced above, the SG technique shown in Fig. 3 has several units, each comprising three electrodes or two dipoles. The electrodes are collinear for the same line, and the lines are parallel. The main difference between the SG and the leapfrog is that there is no common reference electrode among different units. For this reason, the summation procedure present in the leapfrog technique cannot be performed in this case. However, it is important to consider that while the SG technique may have limitations, it also offers advantages in terms of simplicity and efficiency, particularly in scenarios where the conventional techniques may not be feasible. Moreover, it is possible to integrate DERT and SP data simultaneously acquired using the new generation of resistivity meters, with a consequent improvement in the localization of the SP source anomaly. Here, we assume that every unit is independent, but all the units simultaneously measure the p.d. In Fig. 3, 60 acquisition units are represented. In a real field acquisition, this would be equivalent to 2 voltmeters
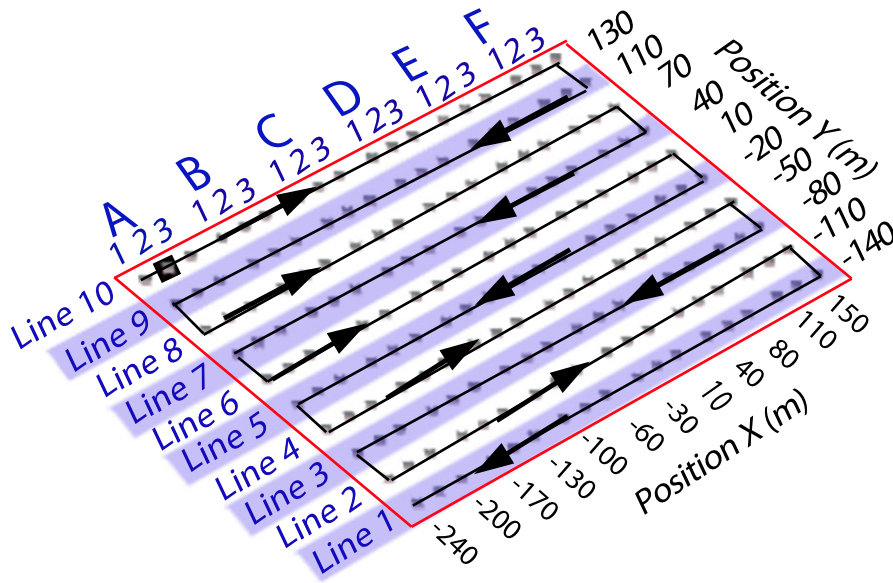
Figure 2. Sequence of dipoles for the measurements of p.d. in the gradient (or leapfrog) and leapfrog with summation techniques. The black square in unit A2 is a reference electrode, labelled as L10A2, meaning 'line 10', position A2, and the arrows indicate the survey orientation.

Table 2. Sequential p.d. in the gradient (or leapfrog) technique for lines 10 and 9, labelled as L10 and L9, respectively.

Potential difference	Potentials
V1	L10A2–L10A1
V2	L10A3–L10A2
V3	L10B1–L10A3
V4	L10B2–L10B1
V5	L10B3–L10B2
. . .	. . .
V18	L9F3–L10F3
V19	L9F2–L9F3
. . .	. . .

per acquisition unit, so 120 voltmeters measure the SP simultaneously. Considering the *X*-direction in Fig. 3, the p.d. was always computed, in the order, between the larger and the lower electrode indices of the same unit, that is, 2–1 and 3–2. For example, in the case of line 10 and positions A and B:

$$V1 = L10A2 - L10A1, \tag{10}$$

$$V2 = L10A3 - L10A2, \tag{11}$$

$$V3 = L10B2 - L10B1, \tag{12}$$

$$V4 = L10B3 - L10B2 \tag{13}$$

and so on. Note that, for the SG technique, only the p.d. can be determined, not the electric potential.
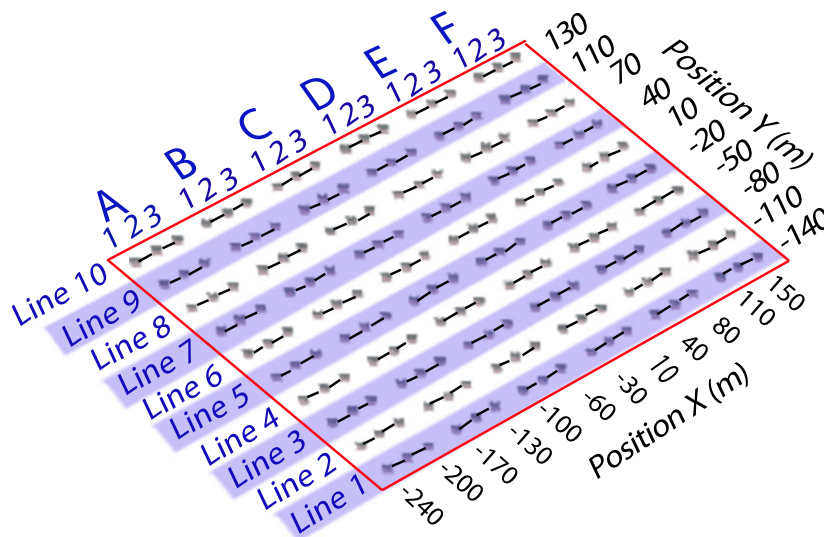
2.4 Full SG technique

The full SG technique employs an 'L' shaped electrode pattern layout, and allows for two horizontal components of the electric field to be measured. As shown in Fig. 4, we adopted both 'L' and 'reversed L' shaped patterns to optimize the spatial resolution.

Considering the *Y*-direction, the p.d. was always computed, in the order, between the larger and the lower line indices, as shown in Table 3. In the *X*-direction, we adopted the same rule of the previous technique, as shown in Table 4.

4 RESULTS

After modelling in COMSOL, the SP at surface were interpolated over the entire survey area shown in Fig. 1(a) using the minimum curvature interpolation method, for all the adopted arrays. Fig. 5 shows the results obtained with a homogeneous background medium and a spherical target with a 10 m radius. The simulated SP shown in Fig. 5(a) are obtained adopting a regular distribution of measurement points (monopoles) spaced by 1 m, that is, it is equivalent to a fixed-base array with the reference electrode placed at very large (theoretically infinite) distance. The fixed-base technique (Fig. 5b) and the leapfrog technique with summation (Fig. 5c) show the same monopolar anomaly, which is similar to that of Fig. 5(a). This is a consequence of the definition of potential, whose analytical expression is eq. (3). The two potential fields (i.e. Figs 5a and b) differ by a constant value, because both the distribution of measurement points and the reference electrode positions are different. The leapfrog technique without summation (Fig. 5d) and the SG technique (Fig. 5e) show a dipolar anomaly, while the full SG technique (Fig. 5f) presented a composition of dipolar response in both directions, *X* and *Y*. The leapfrog technique shows larger SP absolute values than the SG techniques. The SP values of the full SG technique are smaller than those of all the other techniques.

Next, we computed the response of a spherical target of radius 40 m at 150 m depth, adding the five blocky heterogeneities at 5 m depth, as shown in Fig. 1(d). Again, the monopole forward model (Fig. 6a), the fixed-base (Fig. 6b) and the leapfrog with summation techniques (Fig. 6c) are in agreement with each other, producing a monopole anomaly. In contrast, the leapfrog without summation (Fig. 6d) and the SG techniques (Fig. 6e) show a dipole anomaly. Moreover, the full SG technique shows a composition of two dipoles

Figure 3. SG technique, including six different acquisition units labelled from A to F, each unit controlling three electrodes (i.e. two dipoles per acquisition unit), and 10 parallel lines.
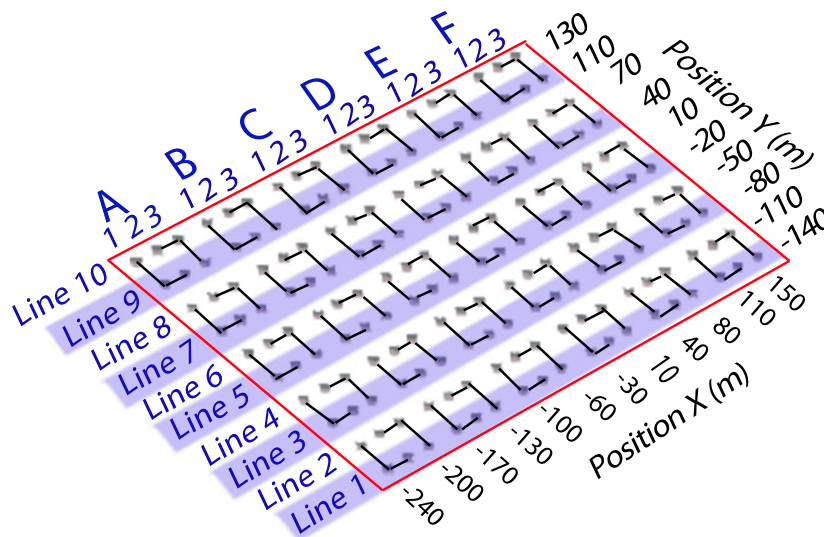
Figure 4. Full SG technique, including orthogonal dipoles for different acquisition units labelled from A to F (direction *X*), comprising three electrodes each. The sequential p.d. in the *Y*-direction for lines 10, 9, . . . , to 1 (also labelled as L10, . . . , L1).

Table 3. Sequential p.d. in the full SG technique—*Y*-direction for lines 10, 9, 5, 4 and 3 (labelled as L10, . . . , L3).

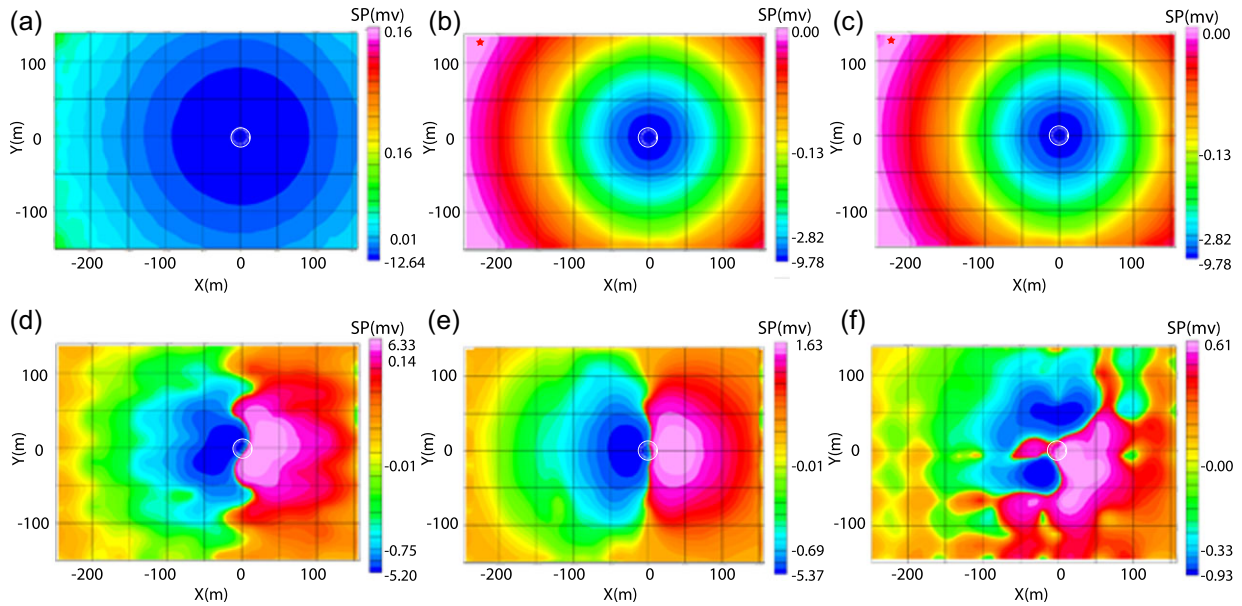| Potential difference	Potentials
V1y	L9A1–L10A1
V2y	L7A1–L8A1
V3y	L5A1–L6A1
. . .	. . .
Vny	L4F3–L3F3
. . .	. . .

Table 4. Sequential p.d. in the full SG technique—*X*-direction for lines 10, 9, 5 and 4 (labelled as L10, . . . , L4).

| Potential difference	Potentials
V1x	L9A2–L9A1
V2x	L10A3–L10A2
V3x	L5A2–L5A1
. . .	. . .
Vnx	L4F3–L4F2
. . .	. . .

in different directions. The spatial resolution is sufficient to locate the blocky heterogeneities (black squares in Figs 6a–c), also those close to the target (white circle in Fig. 6). However, the resolution in Figs 6(d)–(f) is lower due to spatial aliasing. The reduction of measurement points compared to the blocky heterogeneities'

discrepancy leads to spatial aliasing, hiding the accurate representation of smaller variations at the surface shown in Fig. 6.

Note that for the fixed-base, leapfrog with summation and full SG techniques we can appreciate the variation of potential (or p.d.)

Figure 5. Results obtained using a spherical target anomaly with radius 10 m (white circle), for different SP techniques: (a) monopolar anomaly at the surface from the forward modelling, representing the real potential field; (b) fixed-base; (c) leapfrog with summation; (d) leapfrog without summation; (e) SG and (f) full SG. The circles are the sphere projection at the surface. The dots in the left corner (b) and (c) indicate the reference electrode, while the circles are the sphere projection at the surface.
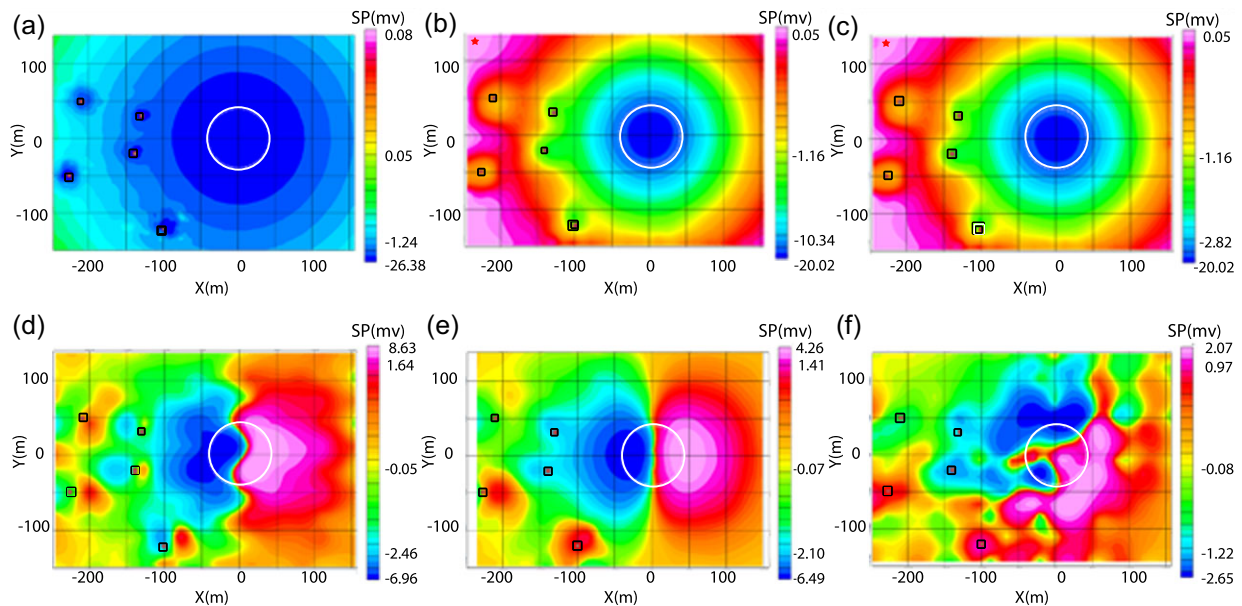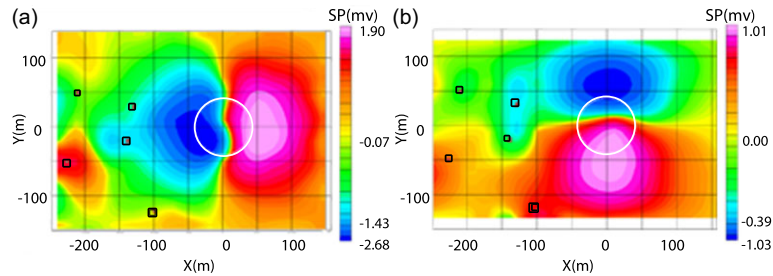

Figure 6. Results obtained using a spherical target anomaly with radius 40 m (white circle) and five blocky heterogeneities, for different SP techniques: (a) monopolar anomaly at the surface from the forward modelling representing the real potential field; (b) fixed-base; (c) leapfrog with summation; (d) leapfrog without summation; (e) SG and (f) full SG. The dots in the left corner (b) and (c) indicate the reference electrode, while the circles are the sphere projection at the surface. Moreover, the black squares indicate the blocky heterogeneities.

in the two directions, while this is not the case for the leapfrog without summation and the SG. For the spherical target radius of 40 m, we plotted in Figs 7(a) and (b) the p.d. of the full SG technique acquired in the *X*- and *Y*-directions, respectively. In both cases, the blocky heterogeneities are not visible (black squares Fig. 7). Although the spherical target generates a monopole anomaly at the surface (Figs 5a and 6a), the full SG technique represents the source anomaly as dipolar in the two perpendicular directions. The dipole orientation is the same as the acquisition direction, that

is, the same as the single electrode dipoles. Then, the composition of the two maps (Fig. 6f) is noisier than the separate plots (Fig. 7). It is important, for the Full SG technique, to interpret the SP maps by plotting the computed p.d. in both directions of acquisition.

Then, we computed the response of the vertical cylinder with sparse blocky heterogeneities. The fixed-base technique (Fig. 8b) agree with the monopole forward modelling (Fig. 8a) but with lower SP magnitude, mainly due to the different spatial distribution of

Figure 7. Results obtained using a spherical target anomaly with radius 40 m (white circle) and five blocky heterogeneities, for the full SG technique. (a) Dipole measurements acquired in the *X*-direction. (b) Dipole measurements acquired in the *Y*-direction. The white circle is the sphere projection at the surface, while the black squares indicate the blocky heterogeneities.
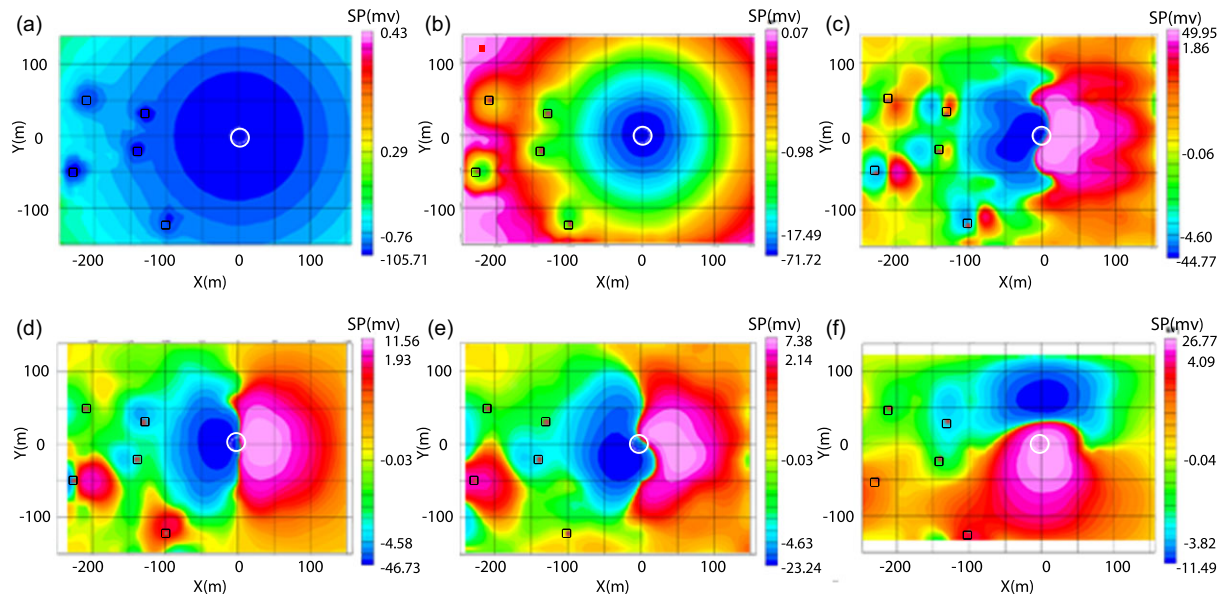
Figure 8. Results obtained using a vertical cylinder with radius 10 m (white circle) and five blocky heterogeneities, for different SP techniques: (a) monopole forward modelling representing the real potential field; (b) fixed-base; (c) leapfrog without summation; (d) SG; (e) full SG in the *X*-direction and (f) full SG in the *Y*-direction. The dot in (b) indicates the reference electrode, while the circle is the cylinder projection at the surface. Moreover, the squares indicate the blocky heterogeneities.

measurement points (denser in Fig. 8a). The resolution is sufficient to distinguish both the deep primary source anomaly and the shallow heterogeneities. As in the previous case, the fixed-base and the leapfrog with summation (not shown in Fig. 8) are the same. Instead, the leapfrog technique without summation (Fig. 8c) and the SG technique (Fig. 8d) shows a dipolar anomaly and the resolution is not sufficient to distinguish the blocky heterogeneities. In the meantime, the full SG technique is a composite of a dipolar anomaly in the *X* (Fig. 8e) and *Y* (Fig. 8f) directions. The response was similar to the spherical model but with a larger magnitude.

For the cylinder dipping 35° in the negative *Y*-direction we obtained a dipole response for the monopole forward modelling (Fig. 9a), the fixed-base technique (Fig. 9b) and the leapfrog technique with a summation (Fig. 9c). Again, the responses were in agreement with each other and with a good resolution. As in the previous cases, the monopole forward modelling exhibits higher SP magnitude, due to the different spatial distribution of measurements points. The leapfrog without summation (Fig. 9d) and the SG technique (Fig. 9e) show a quadrupole response and a low resolution.

On the other hand, the full SG responses in the *X*- and *Y*-directions resemble a quadrupole and two dipoles (of opposite

polarities) in series, respectively, while their composition is unclear. In all cases, the centre of the dipoles or the quadrupoles do not match the exact centre of the cylinder. Only in Figs 9(a)–(c), the resolution is sufficient to image the shallow resistive heterogeneities.

For a dipping cylinder 35° toward the negative *X*-direction, the monopolar forward modelling (Fig. 10a), the leapfrog with summation technique (Fig. 10b) and the fixed-base technique (Fig. 10c) exhibit dipolar anomalies with a positive lobe in the negative *X*-direction, that is, rotated 90° with respect to the previous case. Although the techniques' responses provided different values related to the forward model, their magnitudes are equivalent.

The other techniques provided complicated responses resembling a composition of dipoles with opposite polarities in series.

Gaussian random noise was added to the numerical modelling to obtain more realistic responses. The noise level ranges from 0 to 90 per cent. In the cases described, at a noise level of about 50–60 per cent the results no longer exhibit a clear and distinguishable dipolar (or quadrupolar) anomaly. In the dipping cylinder case, the SG techniques show a loss of resolution in distinguishing the
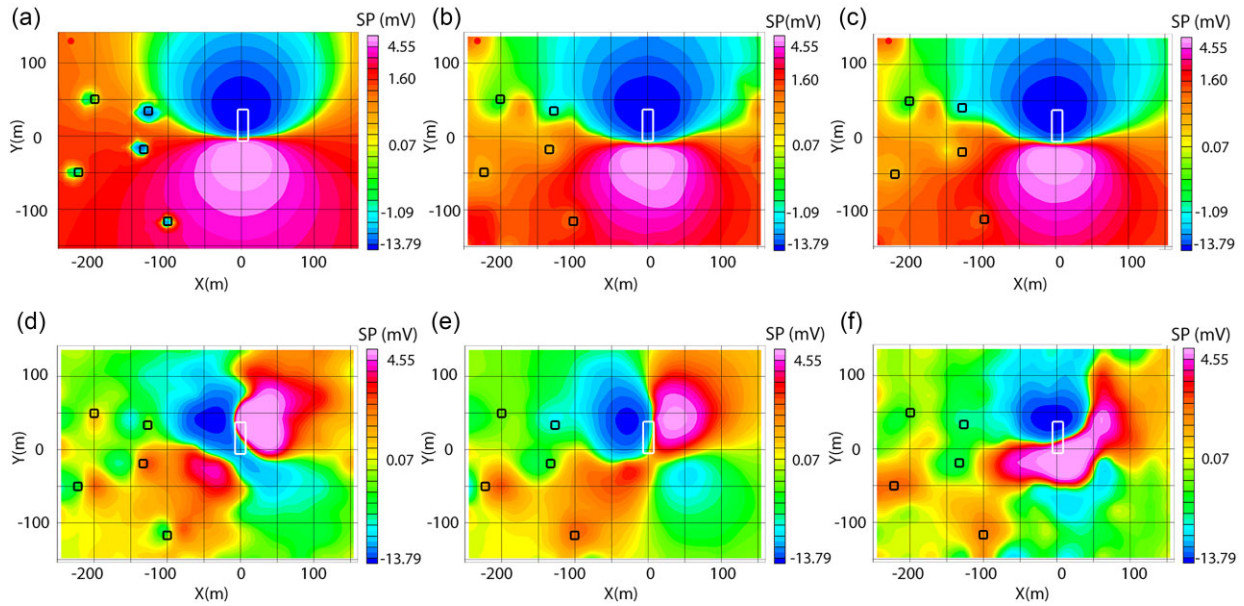
Figure 9. Results obtained using a 35° dipping cylinder (in the negative *Y*-direction) with radius 10 m and five blocky heterogeneities, for different SP techniques: (a) monopole forward modelling representing the real potential field; (b) fixed-base; (c) leapfrog without summation; (d) SG; (e) full SG in the *X*-direction and (f) full SG in the *Y*-direction. The dot in (b) indicates the reference electrode, while the rectangle is the cylinder projection at the surface. Moreover, the squares indicate the blocky heterogeneities.
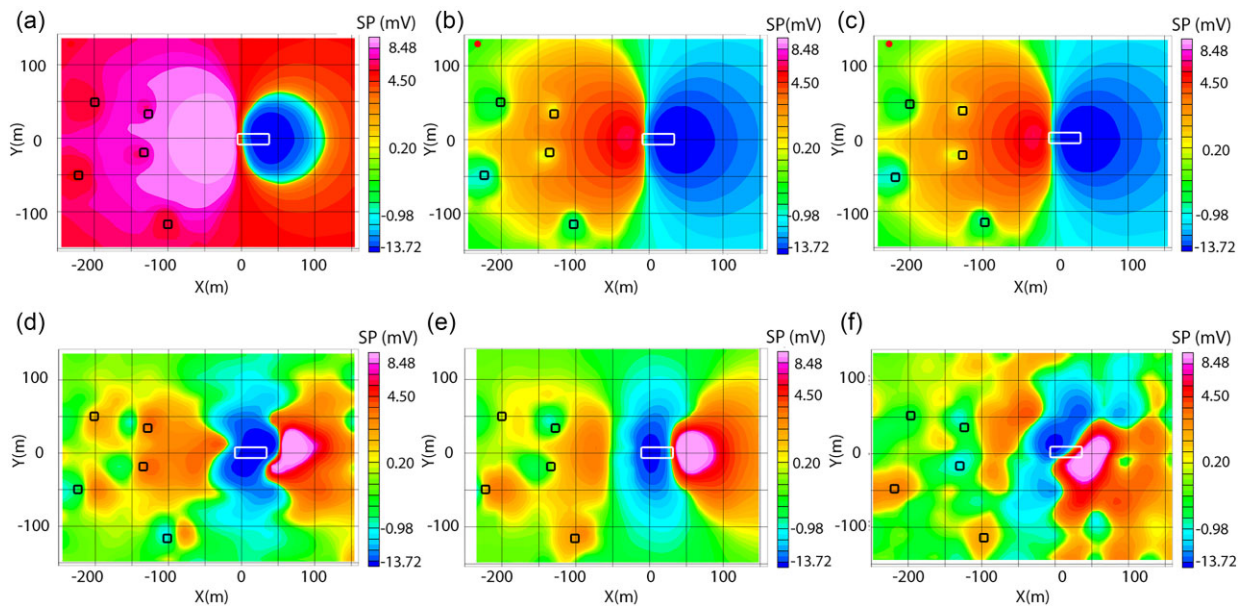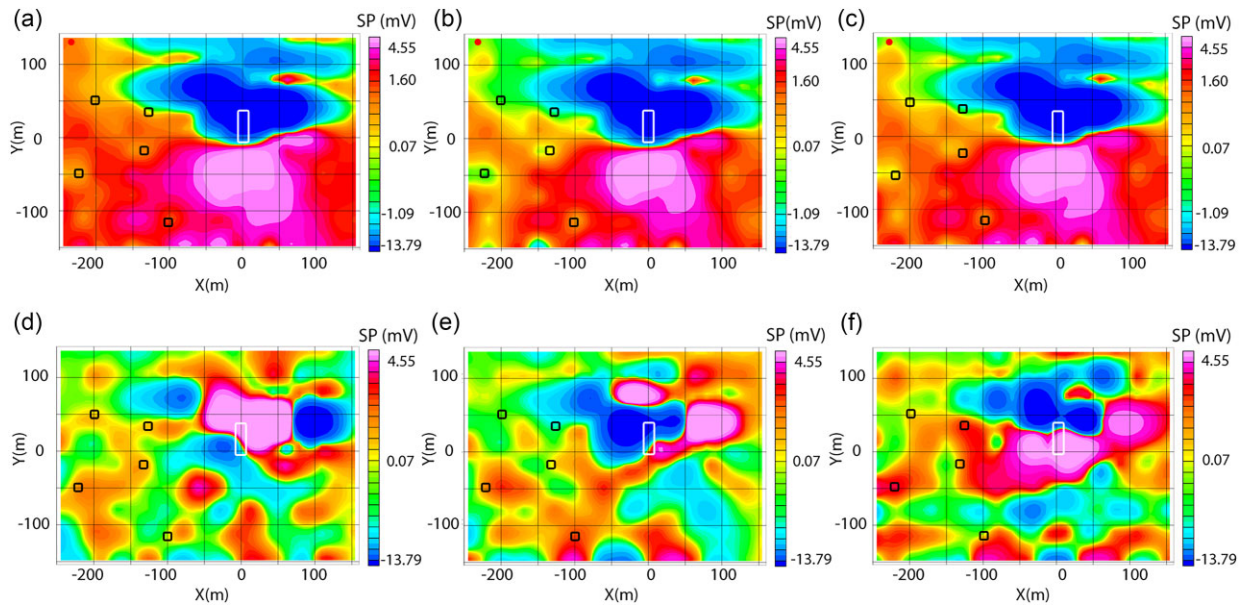

Figure 10. Results obtained using a 35° dipping cylinder (in the negative *X*-direction) with radius 10 m and five blocky heterogeneities, for different SP techniques: (a) monopole forward modelling representing the real potential field; (b) fixed-base; (c) leapfrog with summation; (d) leapfrog without summation; (e) SG and (f) full SG. The dots in (a)–(c) indicate the reference electrode, while the rectangle is the cylinder projection at the surface. Moreover, the squares indicate the blocky heterogeneities.

quadrupole anomaly at even lower noise levels of approximately 40 per cent, except that in the dipping direction, which loses its resolution at 70 per cent.

Fig. 11 shows the results adding 30 per cent Gaussian noise, in the case of dipping cylinder in the *Y*-direction). The leapfrog with summation and fixed-base techniques no longer produce the same response in the presence of random noise. Moreover, the lateral shallow heterogeneities are no longer visible also for the traditional techniques. The leapfrog technique without summation

(Fig. 11d) and the SG technique exhibit the worst results and the responses of the full SG technique are unclear, which could lead to misinterpretation of the source anomaly. Therefore, one must be cautious when interpreting results using these techniques in high-noise areas.

In general, when the reference electrode is placed away from the source anomaly at ground potential, the fixed-base and leapfrog with summation techniques provide the best results.

Figure 11. Results obtained in presence of 30 per cent random noise, using a 35° dipping cylinder (in the negative *Y*-direction) with radius 10 m and five blocky heterogeneities, for different SP techniques: (a) monopole forward modelling representing the real potential field; (b) fixed-base; (c) leapfrog with summation; (d) leapfrog without summation; (e) SG and (f) full SG for both *X*- and *Y*-components. The dots in (a)–(c) indicate the reference electrode, while the rectangle is the cylinder projection at the surface. Moreover, the black squares indicate the blocky heterogeneities.

4.1 Analytical signal amplitude approaches

In the following examples we show how the ASA, described in Section 2.2, can help identify the source anomaly. We show the results of a monopole forward model for a dipping cylinder with a radius of 10 m. As in the previous cases, we adopted a regular distribution of measurement points (monopoles) spaced by 1 m for the plot interpolation, and a reference electrode placed at very large (theoretically infinite) distance. Figs 12(a) and (b) show the amplitude of the electric field, which is calculated by the magnitude of the electric field vector simulated at the surface, while Figs 12(c) and (d) show the ASA computed from the simulated potentials using eq. (5). In both cases, the electric field is well represented by a positive peak centred on the source anomalies (Figs 12a and b). The ASA and electric field maps are in a good agreement, showing similar amplitudes and local differences related to numerical issues around the blocky heterogeneities.

Fig. 13 displays the ASA responses of the different arrays in the case of the cylinder dipping to the negative *Y*-direction. All the techniques successfully delimited the primary source anomaly, except a slight shift in the SG array. Good results were obtained for the cylinder dipping to the negative *X*-direction (Fig. 14) as well as, except a slight mismatch for the full SG technique. In both cylindrical cases, fixed-base and leapfrog with summation techniques provide responses very similar to those of the monopole forward modelling, because the ASA is exactly the electric field modulus when *V* is the potential field in eq. (4). Although the SG is the noisier approach in measuring the p.d, the ASA enables for a great improvement of the response of this array technique (e.g. Fig. 13e). Moreover, the traditional SP arrays undoubtedly provided the best results using ASA as well.

The results of the ASA analysis in the presence of random noise are displayed in Fig. 15, where a 30 per cent noise level has been adopted. The fixed-base and leapfrog with summation techniques show the best performance in terms of source delimitation (Figs 15b and c). In general, the application of the ASA technique improved

the results, even if showing some spatial aliasing, related to the rarefaction of measurement points in the case of the leapfrog technique with summation (Fig. 15c). Furthermore, for the leapfrog without summation (Fig. 15d) and SG (Fig. 15e) techniques the acquisition orientation influenced the ASA estimation in the *X*-direction. On the other hand, the full SG technique employed simultaneously in *X*- and *Y*-directions, enabled to estimate the source anomaly location and its orientation both in noisy (30 per cent noise level) and noise-free simulations. Even with some spatial aliasing (as in precedent cases) in the noisy data, all techniques could still identify and delineate the source anomaly using the ASA. With a noise level higher than 30 per cent, the blocky heterogeneities are hardly detectable.

5 DISCUSSION

We performed a numerical modelling, using the COMSOL package, to compute the SP response of different geological structures and adopting different acquisition techniques. The model was a homogeneous medium with embedded spherical, cylindrical and small blocky heterogeneities.

The results showed that the fixed-base and the leapfrog with summation techniques are comparable with the monopole forward modelling in all the cases considered, showing responses of higher quality with respect to the other techniques. In the spherical and vertical cylinder cases, a monopolar anomaly was generated at the surface. The leapfrog without summation and the SG techniques provided dipolar response, while the Full SG technique presented a composition of dipoles.

In presence of random noise, the fixed-base and the leapfrog techniques show the best performance in resolving shallow resistive heterogeneities. However, adopting the ASA algorithm, also the SG techniques could resolve the blocky resistive bodies until a 30 per cent noise threshold level.
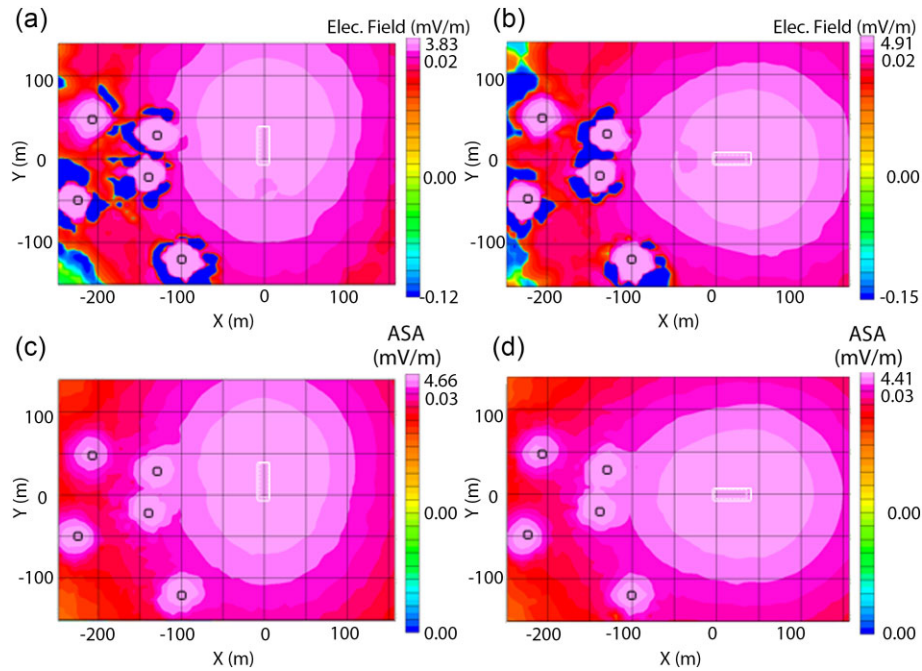
Figure 12. (a) and (b) Normalized electric field and (c) and (d) ASA maps obtained from a monopole forward modelling with a regular distribution of measurement points spaced by 1 m. The target anomaly is a 10 m radius cylinder, dipping 35° (a) and (c) toward negative *Y*-direction and (b) and (d) toward the negative *X*-direction. The white rectangles are the cylinder projections at the surface, while the black squares indicate blocky heterogeneities.
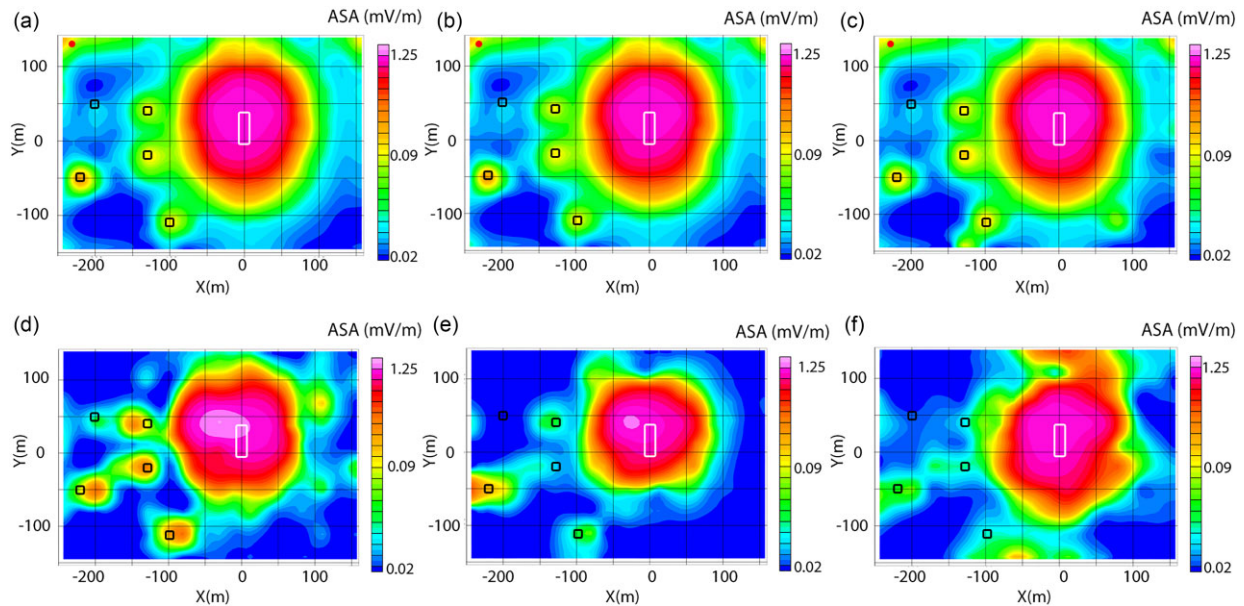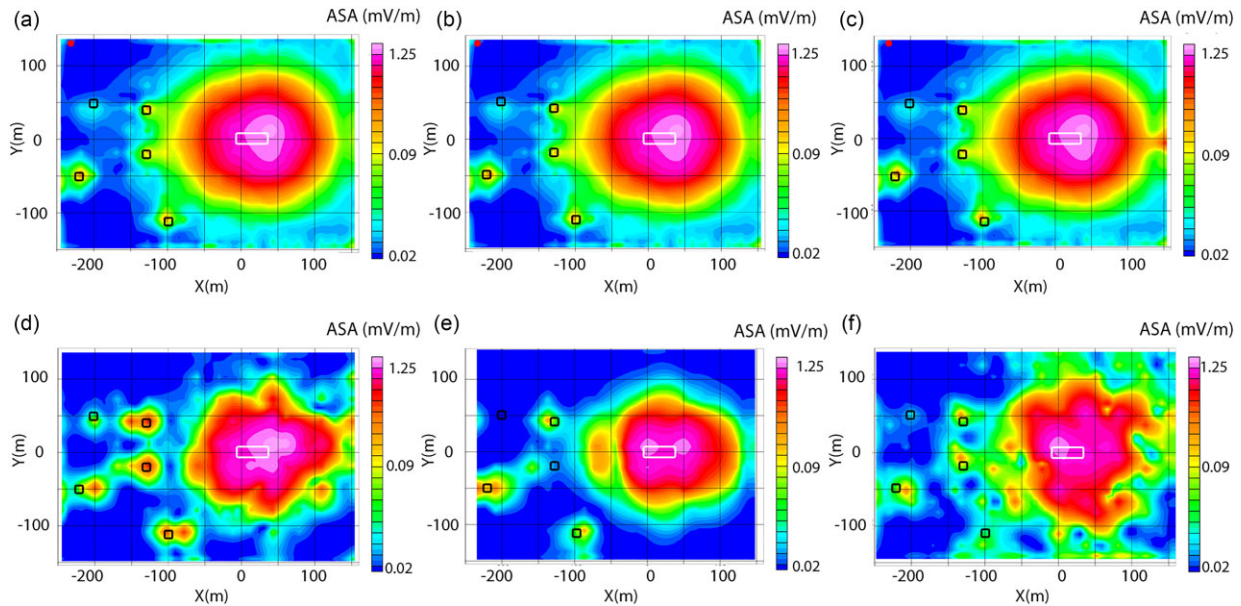
Figure 13. ASA maps for the cylinder dipping to the negative *Y*-direction, for different SP techniques: (a) forward model; (b) fixed-base; (c) leapfrog with summation; (d) leapfrog without summation; (e) SG and (f) full SG. The dots in (a)–(c) indicate the reference electrodes, while the rectangle is the cylinder projection at the surface. Moreover, the squares indicate the blocky heterogeneities.

To analyse the influence of different array techniques and target structures, we considered also a dipping cylindrical body. In this case, a dipolar anomaly was observed in the fixed-base and leapfrog with summation techniques, while in the other techniques, a quadrupole or two combined dipoles were observed. When the acquisition direction is parallel to the cylinder axis, the results of the SG, leapfrog without summation, and full SG techniques are a composition of dipoles in series. However, when the

acquisition direction is orthogonal to the cylinder axis, the results are quadrupoles.

Table 5 presents the root mean square error (RMSE) is expressed in millivolts (mV) for the SP and millivolts per metre (mV m⁻¹) for the ASA results, both in noise-free conditions and with 30 per cent noise added. We calculated the individual squared errors for each SP and ASA results. Then, we computed the square root of the average of the squared errors (RMSE). The fixed-base and leapfrog

Figure 14. ASA maps for the cylinder dipping to the negative *X*-direction, for different SP techniques: (a) forward model; (b) fixed-base; (c) leapfrog with summation; (d) leapfrog without summation; (e) SG and (f) full SG. The dots in (a)–(c) indicate the reference electrode, while the rectangle is the cylinder projection at the surface. Moreover, the squares indicate the blocky heterogeneities.
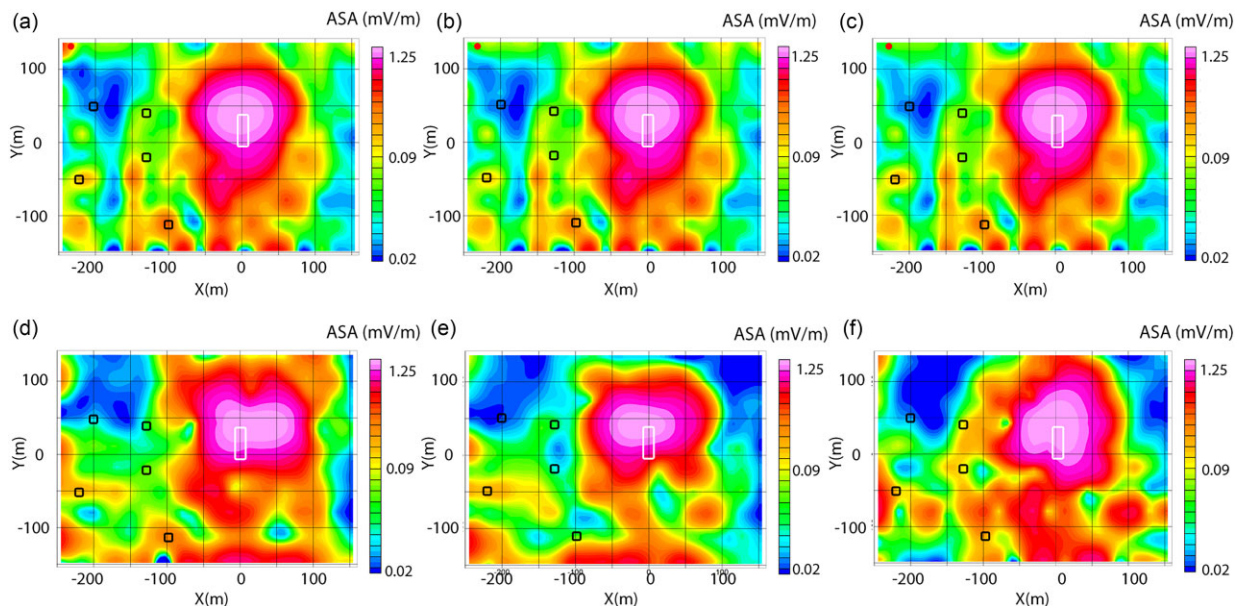
Figure 15. ASA maps with 30 per cent random noise for the cylinder dipping to the negative *Y*-direction, for different SP techniques: (a) monopole forward modelling; (b) fixed-base; (c) leapfrog with summation; (d) leapfrog without summation; (e) SG and (f) Full SG. The dots in (a)–(c) indicate the reference electrode, while the rectangle is the cylinder projection at the surface. Moreover, the squares indicate the blocky heterogeneities.

with summation techniques are equivalent and represent the optimal choices for obtaining high-resolution SP maps and accurately locating primary and shallow source anomalies. However, excellent results can also be achieved using the SG and full SG arrays with the support of the ASA methodology, allows to obtain valuable additional SP information that would otherwise be discarded in standard DERT processing procedures.

The application of ASA on fixed-base and leapfrog with summation techniques reduced the error from 0.83 to 0.15 for the noise free case. Similarly, for the leapfrog without summation technique, the error decreased from 8.30 to 0.44, while for the SG

technique decreased from 6.56 to 0.42. The ASA error for the full SG technique was approximately 0.46. For the cases with 30 per cent added noise, the values changed as follows: from 1.65 to 0.04 for fixed-base, from 14.31 to 0.37 for leapfrog without summation, from 1.55 to 0.03 for leapfrog with summation, from 10.87 to 0.29 for SG and from 9.66 to 0.22 for full SG. These findings show that the ASA procedure considerably improved the reliability of the information regarding source anomalies delimitation.

Regardless of the performance of the individual array, new-generation resistivity meters allow to speed up the acquisition time

Table 5. RMSE of the SP (Figs 9 and 11) and ASA (Figs 13 and 15) using different arrays, in comparison with the forward model. The noise-free and noisy conditions, with 30 per cent noise added, are considered.

		SP (mV)				
Arrays		Fixed-base	Leapfrog without sum	Leapfrog with sum	SG	Full SG
Noise free	RMSE	0.83	8.30	0.84	6.56	4.93
Noise 30 per cent	RMSE	1.65	14.31	1.55	10.87	9.66
		ASA (mV/m)				
Arrays		Fixed-base	Leapfrog without sum	Leapfrog with sum	SG	Full SG
Noise free	RMSE	0.15	0.44	0.16	0.42	0.46
Noise 30 per cent	RMSE	0.04	0.37	0.03	0.29	0.22

and to adopt multiple acquisition techniques in the same SP survey, increasing the information content of SP data. These instruments usually employ SG arrays, but can be adapted also to the traditional arrays. For example, the fixed-base and leapfrog with summation techniques can be easily employed, with some precautions, using the new generation resistivity meters. This development leads to a significant improvement in the estimate of the electric fields and in a more reliable definition of source anomalies.

It is important to note that most DERT acquisitions utilize stainless steel electrodes rather than non-polarizing electrodes. In many industrial DERT systems, such as the FullWaver, the receiving electrodes are not used for current injection. This physical separation between the transmitting and receiving electrodes significantly reduces the polarization effect associated with stainless-steel electrodes. Typically, a bias is observed between the SP amplitudes recorded with stainless steel and non-polarizing electrodes. However, this residual polarization can be further mitigated through advanced processing techniques. Consequently, the overall SP maps appear very similar, allowing for the clear identification of the primary source anomaly in both cases (stainless steel and non-polarizing electrodes, such as PbCl2/Pb). The differences are mainly in the amplitude, which varies slightly.

6 CONCLUSIONS

We carried out a series of finite-element numerical simulations, using the COMSOL software package, to calculate SP maps in different settings and with various acquisition techniques. Spherical, cylindrical and blocky targets were included in a homogeneous background, thus creating several subsurface models. Modelling results clearly show that the fixed-base and the leapfrog summation techniques are equivalent and they outline different sources of anomaly with a high degree of resolution. Contrarily, the responses of the leapfrog without summation and of the SG techniques are not straightforward to interpret, in particular in cases with noisy data. For this reason, the summation procedure, in the leapfrog technique, is highly recommended as it provides more reliable results leading to a better interpretation. The ASA maps, showing a single peak centred over the targets, can significantly help in identifying the source anomalies for all the analysed array techniques. In particular, the application of ASA greatly improved the SG responses for all the considered cases, providing reliable information about the electric field generated by the anomaly sources and delimitating the target position at the surface, also in presence of random noise.

As expected, the fixed-base and the leapfrog techniques with summation are the best survey choice for SP mapping due to their better accuracy and to their higher resolution in outlining the anomaly

sources. However, the SG techniques also provided excellent and interpretable responses when adopting the ASA algorithm, comparable to the results obtained with traditional arrays. This is a relevant breakthrough as it paves the way to a systematic use of SP maps in DERT surveys. This is particularly true in case of separation between the transmission line and the receivers. The typical 3-D layout, when collecting DERT data, could be assumed as a non-conventional array and it could be exploited to obtain additional information on the SP maps, enabling a comprehensive electrical characterization of the subsurface. A careful design of DERT field geometry allows for this novel integrated exploration approach especially in cases of large deployments of new-generation distributed systems with several potential-logging units. This approach is cost-effective in terms of both time and logistical effort and, as proved in this study, it could provide additional insight in imaging the subsurface.

DECLARATION OF COMPETING INTEREST

The authors declare that they have no known competing financial interests or personal relationships that could have appeared to influence the work reported in this paper.

DATA AVAILABILITY

Data will be made available on request.

REFERENCES

AB COMSOL, 2017. *COMSOL Multiphysics® v. 5.3*. COMSOLAB, Stockholm, Sweden, https://doi.org/www.comsol.com

Abdelrahman, E.M., El-Araby, T.M. & Essa, K.S., 2009. Shape and depth determinations from second moving average residual self-potential anomalies, *J. geophys. Eng.,* **6**(1), 43–52.

Abdelrahman, E.S.M., El-Araby, H.M., Hassaneen, A.R.G. & Hafez, M.A., 2003. New methods for shape and depth determinations from SP data, *Geophysics,* **68**(4), 1202–1210.

Abedi, M., Hafizi, M.K. & Norouzi, G.H., 2012. 2D interpretation of self-potential data using normalized full gradient, a case study: galena deposit, *Boll. Geofis. Teor. Appl.,* **53**(2), doi: 10.4430/bgta0053.

Agarwal, B.N.P. & Srivastava, S., 2009. Analyses of self-potential anomalies by conventional and extended Euler deconvolution techniques, *Comput. Geosci.,* **35**(11), 2231–2238.

Agarwal, B.N.P., 1984. Quantitative interpretation of self-potential anomalies, in *SEG Technical Program Expanded Abstracts 1984,* pp. 154–157, Society of Exploration Geophysicists.

Ahmed, A.S., Revil, A., Bolève, A., Steck, B., Vergniault, C., Courivaud, J.R., Jougnot, D. & Abbas, M., 2020. Determination of the permeability of seepage flow paths in dams from self-potential measurements, *Eng. Geol.,* **268**, 105514, doi:10.1016/j.enggeo.2020.105514.

Atchuta Rao, D. & Ram Babu, H.V., 1983. Quantitative interpretation of self-potential anomalies due to two-dimensional sheet-like bodies, *Geophysics,* **48**(12), 1659–1664.

Auken, E., Guérin, R., de Marsily, G. & Sailhac, P., 2010. Comment on "Review of self-potential methods in hydrogeophysics" by L. Jouniaux et al.[CR Geoscience 341 (2009) 928–936], *C. R. Géosci.,* **342**(10), 806, doi: 10.1016/j.crte.2010.06.001.

Barde-Cabusson, S., Finizola, A. & Grobbe, N., 2021. A practical approach for self-potential data acquisition, processing, and visualization, *Interpretation,* **9**(1), T123–T143.

Beiki, M., 2010. Analytic signals of gravity gradient tensor and their application to estimate source location, *Geophysics,* **75**(6), I59–I74.

Biswas, A., 2017. A review on modeling, inversion and interpretation of self-potential in mineral exploration and tracing paleo-shear zones, *Ore Geol. Rev.,* **91**, 21–56.

Biswas, A., 2019. Inversion of amplitude from the 2-D analytic signal of self-potential anomalies, *Minerals,* https://doi.org/10.5772/intechopen.79111.

Bocchia, F., Francese, R.G., Giorgi, M., Fischanger, F. & Picotti, S., 2021. The impact of multiple transmitters on the signal strength in Deep Electrical Resistivity Tomography data: an experiment in the Vajont valley (north-eastern Italy), *Boll. Geofis. Teor. Appl.,* **62**(4) 687–706.

Bolève, A., Revil, A., Janod, F., Mattiuzzo, J.L. & Jardani, A., 2007. Forward modeling and validation of a new formulation to compute self-potential signals associated with ground water flow, *Hydrol. Earth Syst. Sci.,* **11**(5), 1661–1671.

Carrier, A., Fischanger, F., Gance, J., Cocchiararo, G., Morelli, G. & Lupi, M., 2019. Deep electrical resistivity tomography for the prospection of low-to medium-enthalpy geothermal resources, *Geophys. J. Int.,* **219**(3), 2056–2072.

Eppelbaum, L.V., 2021. Advanced Analysis of Self-potential Anomalies: Review of Case Studies from Mining, Archaeology and Environment, *Self-Potential Method: Theoretical Modeling and Applications in Geosciences Springer Geophysics,* 203–248.

Finizola, A., Lénat, J.F., Macedo, O., Ramos, D., Thouret, J.C. & Sortino, F., 2004. Fluid circulation and structural discontinuities inside Misti volcano (Peru) inferred from self-potential measurements, *J. Volc. Geotherm. Res.,* **135**(4), 343–360.

Gance, J., Leite, O., Texier, B., Bernard, J. & Truffert, C., 2018. The Fullwaver systems: distributed network of autonomous devices for deep 3D electrical resistivity and induced polarization survey, *Geophysical Research Abstracts,* **20**, EGU2018–12569.

Gibert, D. & Sailhac, P., 2008. Comment on" self-potential signals associated with preferential groundwater flow pathways in sinkholes by A. Jardani, JP Dupont, and A. Revil, *J. geophys. Res.: Solid Earth,* **113**(3), B03210, doi:10.1029/2007JB004969.

Griffiths, D.J., 1999. *Introduction to Electrodynamics,* 3rd edn, Pearson/Addison-Wesley, p. 213.

Ikard, S.J., Briggs, M.A. & Lane, J.W., 2021. Investigation of scale-dependent groundwater/surface-water exchange in rivers by gradient self-potential logging: numerical modeling and field experiments, *J. Environ. Eng. Geophys.,* **26**(2), 83–98.

Jardani, A., Revil, A. & Dupont, J.P., 2006. Self-potential tomography applied to the determination of cavities, *Geophys. Res. Lett.,* **33**(13), doi:10.1029/2006GL026028.

Jiang, K., Zheng, P., Chen, M., Xiao, B., Zhang, C. & Chen, K., 2024. Low-noise multi-channel underwater electric field measurement and analysis system for a ship model, *Rev. Sci. Instrum.,* **95**(1), doi:10.1063/5.0 171389.

Jouniaux, L., Maineult, A., Naudet, V., Pessel, M. & Sailhac, P., 2009. Review of self-potential methods in hydrogeophysics, *C.R. Geosci.,* **341**(10-11), 928–936.

Jouniaux, L., Maineult, A., Naudet, V., Pessel, M. & Sailhac, P., 2010. Reply to the comment by A. Revil on "Review of self-potential methods in hydrogeophysics" by L. Jouniaux et al.[CR Geoscience 341 (2009) 928–936], *C. R. Géosci.,* **342**(10), 810–813.

Kang, X., Kokkinaki, A., Kitanidis, P.K., Shi, X., Revil, A., Lee, J., Ahmed, A.S. & Wu, J., 2020. Improved characterization of DNAPL source zones via sequential hydrogeophysical inversion of hydraulic-head, self-potential and partitioning tracer data, *Water Resour. Res.,* **56**(8), e2020WR027627, doi:10.1029/2020WR027627.

Kukemilks, K. & Wagner, J.F., 2021. Detection of preferential water flow by electrical resistivity tomography and self-potential method, *Appl. Sci.,* **11**(9), 4224, doi:10.3390/app11094224.

LaBrecque, D.J., Morelli, G., Fischanger, F., Lamoureux, P. & Brigham, R., 2013. Field trials of the multi-source approach for resistivity and induced polarization data acquisition, in *AGU Fall Meeting Abstracts,* Vol., **2013**, pp. NS34A–03, American Geophysical Union (AGU), San Francisco, CA, USA.

Lajaunie, M., Gance, J., Nevers, P., Malet, J.P., Bertrand, C., Garin, T. & Ferhat, G., 2019. Structure of the Séchilienne unstable slope from large-scale 3D electrical tomography using a Resistivity distributed automated System (R-DAS), *Geophys. J. Int.,* **219**(1), 129–147.

Li, X., 2006. Understanding 3D analytic signal amplitude, *Geophysics,* **71**(2), L13–L16.

Mehanee, S. A., Essa, K. S., Soliman, K. S. & Diab, , Z.E. 2023 A fast imaging method for the interpretation of self-potential data with application to geothermal systems and mineral investigation.*Scientific Reports* **13(1)**, 13548, doi:10.1038/s41598-023-39672-8.

Mehanee, S.A., 2014. An efficient regularized inversion approach for self-potential data interpretation of ore exploration using a mix of logarithmic and non-logarithmic model parameters, *Ore Geol. Rev.,* **57**, 87–115.

Meiser, P., 1962. A method for quantitative interpretation of self-potential measurements, *Geophys. Prospect.,* **10**(2), 203–218.

Mendonça, C.A., 2008. Forward and inverse self-potential modeling in mineral exploration, *Geophysics,* **73**(1), F33–F43.

Minsley, B.J., Sogade, J. & Morgan, F.D., 2007. Three-dimensional source inversion of self-potential data, *J. geophys. Res.: Solid Earth,* **112**, doi:10.1029/2006JB004262.

Monteiro Santos, F.A., 2010. Inversion of self-potential of idealized bodies' anomalies using particle swarm optimization, *Comput. Geosci.,* **36**(9), 1185–1190.

Nabighian, M.N., 1972. The analytic signal of two-dimensional magnetic bodies with polygonal cross-section, its properties and use for automated anomaly interpretation, *Geophysics,* **37**, 507–517.

Nyquist, J.E. & Corry, C.E., 2002. Self-potential: the ugly duckling of environmental geophysics, *Leading Edge,* **21**(5), 446–451.

Orellana, E., 1972. *Prospección Geoeléctrica en corriente continua,* Vol., **1**. Madrid: Paraninfo.

Patella, D., 1997. Introduction to ground surface self-potential tomography, *Geophys. Prospect.,* **45**(4), 653–681.

Paul, M.K., 1965. Direct interpretation of self-potential anomalies caused by inclined sheets of infinite horizontal extensions, *Geophysics,* **30**(3), 418–423.

Picotti, S., Francese, R., Giorgi, M., Pettenati, F. & Carcione, J.M., 2017. Estimation of glaciers thicknesses and basal properties using the horizontal-to-vertical component spectral ratio (HVSR) technique from passive seismic data, *J. Glaciol.,* **63**, 229–248.

Poldini, E., 1938. Geophysical exploration by spontaneous polarization methods, *Min. Mag.,* 59, 278–282.

Rakoto, H.A., Rajaomahefasoa, R., Razafiarisera, R. & Razafindrakoto, B., 2019. Evaluation of flake graphite ore using self-potential (SP), electrical resistivity tomography (ERT) and induced polarization (IP) methods in east coast of Madagascar, *J. appl. Geophys.,* **169**, 134–141.

Rao, B.S.R., Murthy, I.R. & Reddy, S.J., 1970. Interpretation of self-potential anomalies of some simple geometric bodies, *Pure appl. Geophys.,* **78,** 66–77.

Revil, A. & Jardani, A., 2013. *The Self-Potential Method: Theory and Applications in Environmental Geosciences*. Cambridge University Press, Cambridge.

Revil, A., 2010. Comment on "Review of self-potential methods in hydrogeophysics" by L. Jouniaux et al.[CR Geoscience 341 (2009) 928–936], *C. R. Géosci.,* **342**(10), 807–809.

Revil, A., Finizola, A. & Gresse, M., 2023a. Self-potential as a tool to assess groundwater flow in hydrothermal systems: a review, *J. Volc. Geotherm. Res.,* **437,** 107788, doi:10.1016/j.jvolgeores.2023.107788.

Revil, A., Jardani, A. & Dupont, J.P., 2008. Reply to comment by D. Gibert and P. Sailhac on "Self-potential signals associated with preferential groundwater flow pathways in sinkholes, *J. geophys. Res.,* **113,** B03205, doi:10.1029/2007JB005396.

Revil, A., Su, Z., Zhu, Z. & Maineult, A., 2023b. Self-potential as a tool to monitor redox reactions at an ore body: a sandbox experiment, *Minerals,* **13**(6), 716, doi:10.3390/min13060716.

Revil, A., Titov, K., Doussan, C. & Lapenna, V., 2006. Applications of the self-potential method to hydrological problems, in Applied Hydrogeophysics, eds, Vereecken, H., Binley, A., Cassiani, G., Revil, A. & Titov, K., vol. 71. Springer, Dordrecht, NATO Science Series.

Roest, W.R., Verhoef, J. & Pilkington, M., 1992. Magnetic interpretation using the 3-D analytic signal, *Geophysics,* **57**(1), 116–125.

Roudsari, M.S. & Beitollahi, A., 2013. Forward modelling and inversion of self-potential anomalies caused by 2D inclined sheets, *Explor. Geophys.,* **44**(3), 176–184.

Sheffer, M.R. & Oldenburg, D.W., 2007. Three-dimensional modelling of streaming potential, *Geophys. J. Int.,* **169,** 839–848.

Sill, W.R., 1983. Self-potential modeling from primary flows, *Geophysics,* **48**(1), 76–86.

Sindirgi, P. & Özyalin, Ş., 2019. Estimating the location of a causative body from a self-potential anomaly using 2D and3D normalized full gradient and Euler deconvolution, *Turk. J. Earth Sci.,* **28**(4), 640–659.

Sindirgi, P., Pamukçu, O. & Özyalın, Ş., 2008. Application of normalized full gradient method to self-potential (SP) data, *Pure appl. Geophys.,* **165,** 409–427.

Song, S., Deng, X., Su, Z., Deng, M. & Chen, K., 2022. Marine self-potential measurement tool for autonomous underwater vehicle, *Rev. Sci. Instrum.,* **93**(11), doi:10.1063/5.0098079.

Song, S.Y., Cho, A., Kang, P.K. & Nam, M.J., 2021. A review on past cases of self-potential surveys for dikes and embankments considering streaming potential, *J. Soil Groundwater Environ.,* **26**(6), 1–17.

Soueid Ahmed, A., Jardani, A., Revil, A. & Dupont, J.P., 2016. Joint inversion of hydraulic head and self-potential data associated with harmonic pumping tests, *Water Resour. Res.,* **52**(9), 6769–6791.

Su, Z. *et al.*, 2022 3D self-potential tomography of seafloor massive sulfide deposits using an autonomous underwater vehicle, *Geophysics,* **87**(4), B255–B267.

Sundararajan, N. & Srinivas, Y., 1996. A modified hilbert transform and its application to self-potential interpretation, *J. appl. Geophys.,* **36**(2-3), 137–143.

Sundararajan, N., Srinivas, Y. & Rao, T.L., 2000. Sundararajan Transform-A tool to interpret potential field anomalies, *Explor. Geophys.,* **31**(4), 622–628.

Sundararajan, N., Srinivasa Rao, P. & Sunitha, V., 1998. An analytical method to interpret self-potential anomalies caused by 2-D inclined sheets, *Geophysics,* **63**(5), 1551–1555.

Sunny, A.A., 2018. Derivatives and analytic signals: improved techniques for lithostructural classification, *Malaysian J. Geosci.,* **2**(1), 01–08.

Troiano, A., Di Giuseppe, M.G., Monetti, A., Patella, D., Troise, C. & De Natale, G., 2017. Fluid injection in enhanced geothermal systems: a study on the detectability of self-potential effects and on their correlation with induced seismicity, *Geothermics,* **65,** 280–294.

Troiano, A., Isaia, R., Di Giuseppe, M.G., Tramparulo, F.D.A. & Vitale, S., 2019. Deep electrical resistivity tomography for a 3D picture of the most active sector of Campi Flegrei caldera, *Sci. Rep.,* **9**(1), 1–10.

Valois, R., Cousquer, Y., Schmutz, M., Pryet, A., Delbart, C. & Dupuy, A., 2018. Characterizing stream-aquifer exchanges with self-potential measurements, *Groundwater,* **56**(3), 437–450.

Xie, J., Cui, Y.A., Guo, Y., Zhang, L., Fanidi, M. & Liu, J., 2020. 2.5 D self-potential forward modeling by natural-infinite element coupling method, *J. appl. Geophys.,* **179,** 104077.

Xie, J., Cui, Y.A., Liu, J.X., Guo, Y.J., Zhang, L.J., Luo, Y.J. & Zhang, P.F., 2023. A review on theory, modeling, inversion, and application of self-potential in marine mineral exploration, *Trans. Nonferr. Met. Soc. China,* **33**(4), 1214–1232.

Zhu, Z. *et al.*, 2023. 3D Multicomponent self-potential inversion: theory and application to the exploration of seafloor massive sulfide deposits on mid-ocean ridges, *Minerals,* **13**(8), 1098, doi:10.3390/min 13081098.

Zhu, Z., Shen, J., Tao, C., Deng, X., Wu, T., Nie, Z., Wang, W. & Su, Z., 2021. Autonomous-underwater-vehicle-based marine multicomponent self-potential method: observation scheme and navigational correction, *Geosci. Instrum. Methods Data Syst.,* **10**(1), 35–43.